Research Article | Vol. 10, No. 7 | 1 Jul 2019 | BIOMEDICAL OPTICS EXPRESS 3369
Biomedical Optics EXPRESS

Enhanced near infrared optical access to the brain with a transparent cranial implant and scalp optical clearing

MILDRED S. CANO-VELÁZQUEZ,[1,*] NAMI DAVOODZADEH,[2] DAVID HALANEY,[2] CARRIE R. JONAK,[3] DEVIN K. BINDER,[3] JUAN HERNÁNDEZ-CORDERO,[1] AND GUILLERMO AGUILAR[2]

[1]*Instituto de Investigaciones en Materiales, Universidad Nacional Autónoma de México, México*
[2]*Department of Mechanical Engineering, University of California, Riverside, CA, USA*
[3]*Division of Biomedical Sciences, School of Medicine, University of California, Riverside, CA, USA*
[*]*mildred.cano.vel@gmail.com*

Abstract: We report on the enhanced optical transmittance in the NIR wavelength range (900 to 2400 nm) offered by a transparent Yttria-stabilized zirconia (YSZ) implant coupled with optical clearing agents (OCAs). The enhancement in optical access to the brain is evaluated upon comparing *ex-vivo* transmittance measurements of mice native skull and the YSZ cranial implant with scalp and OCAs. An increase in transmittance of up to 50% and attenuation lengths of up to 2.4 mm (i.e., a five-fold increase in light penetration) are obtained with the YSZ implant and the OCAs. The use of this ceramic implant and the biocompatible optical clearing agents offer attractive features for NIR optical techniques for brain theranostics.

1. Introduction

The brain is protected by different tissue layers, each of them having different optical properties (e.g., refractive index contrast, scattering and absorption); hence, the analysis of the spectral features provide information about these different layers [1]. Furthermore, it has been shown that physiological changes in the different head tissues produce variations in their optical properties thereby changing the spectral features of the transmitted and reflected light [2]. Compared to visible light, some spectral regions in the Near Infrared (NIR) spectral range (800 to 2500 nm) offers advantages such as reduced scattering and absorption as well as a deeper penetration depth in tissue media [2–4]. Because of these features, some spectral windows within the NIR wavelength range have shown promising results for brain studies, including deep imaging, diagnostics and therapeutic applications in brain diseases [5–8].

Different optically transparent windows for head tissues have been identified within the NIR spectral range. These wavelength windows avoid light attenuation by the tissue due to water absorption peaks located at 1450 nm and 1940 nm [1,9,10]. The first window NIR-I (~ 700 – 1000 nm), or conventional window, has been well characterized and studied for most tissues, including brain and other soft tissues [1]. Two additional optical windows have been also identified: NIR-II (~ 1000 – 1350 nm) and NIR -III, or short -wave infrared SWIR, (~ 1550 – 1870 nm); the latter spectral region has shown to provide maximum light penetration for some kinds of tissues [7, 11, 12]. More recently, a fourth optical window, SWIR-II (~ 2100 – 2300 nm) has allowed for improved optical studies of the brain and for deep brain imaging, particularly when compared to the NIR -II window [8]. All of these spectral regions have been explored for many biophotonic applications, although the NIR windows have particularly shown excellent potential for noninvasive through-skull *in vivo* brain imaging and spectroscopy [6, 7, 11, 13]. Nonetheless, it is always desirable to reduce the highly scattering cranial bone over the cortex, which hinders the observation of optical signals deriving from deeper tissues and reduce the light penetration

#360539 https://doi.org/10.1364/BOE.10.003369
Journal © 2019 Received 20 Feb 2019; revised 12 May 2019; accepted 29 May 2019; published 14 Jun 2019

Biomedical Optics EXPRESS

distance.

Reduction of the scattering from the skull has been addressed in animal models by craniotomy [14–16], using a thinned-skull cranial physical window [17, 18] or by polishing and reinforcing a thinned skull piece [19]. Other approaches include optical clearing of the skull [20–22], or replacement of a portion of the skull with a physical transparent window made from glass or PDMS [23–25]. All of these are powerful research techniques, but not adequate for translation into human applications that may require permanent cranial implants. While skull thinning and polishing techniques affect the required protection for the brain, glass-based physical windows have a very low toughness ($KIC = 0.7 - 0.9MPa \cdot m^{\frac{1}{2}}$) [26] increasing the potentiality of catastrophic failure by fracture. Similarly, the effects of skull optical clearing agents for long-term use on human skull is still unknown. A number of biomedical considerations including biocompatibility, mechanical strength, and ageing performance must be considered for a physical window intended for eventual clinical applications. Conventional cranial prosthesis including titanium, alumina, and acrylic [27], do not provide the desired combination of transparency and toughness required for clinically-viable transparent cranial implants. Other materials such as sapphire have been also proposed as implants owing to its broadband transparency and toughness thereby providing optical access to the brain [28]. We have recently also introduced a transparent nanocrystalline yttria-stabilized-zirconia cranial implant material showing suitable mechanical strength and biocompatibility sought for a clinically-viable permanent cranial implant for patients [29–31]. Yttria-stabilized zirconia (YSZ) is an attractive alternative due to its relatively high fracture toughness ($KIC \sim 8MPa \cdot m^{\frac{1}{2}}$) [32], as well as its proven biocompatibility in dental and orthopedic applications [33–35]. By performing biocompatibility and ageing tests, and through imaging techniques such as optical coherence tomography [29], ultrasound transmission [36], multi-wavelength intrinsic optical signal imaging [37] and Laser Speckle Imaging (LSI) [38, 39], we have demonstrated the feasibility of YSZ implants for chronic cortical imaging in an acute murine model. Thus, YSZ holds as a promising platform for developing optically transparent implants with excellent potential for human applications.

In this paper, we report on the enhancement in optical access provided by the transparent YSZ implant for brain studies in the NIR wavelength range. Because this cranial implant is sought as a means to obtain optical access for post-operatory and prolonged diagnostics and/or therapy purposes, scalp scattering must be overcome. In this context, we also evaluate the use of optical clearing agents (OCAs) in the scalp, particularly their effects on the optical transmittance in the NIR spectral range. As shown in previous reports, OCAs provide greater optical probing depths and better contrast, as well as improved light focusing and spatial resolution [40–42]. Therefore, evaluation of the optical features of the YSZ implant together with the use of OCAs in the NIR spectral range will provide useful information for theranostics applications operating in this wavelength range (e.g., photobiomodulation [43–45], NIR and fluorescence imaging [3, 46], cancer diagnosis [47, 48] and brain edema [49]). Hence, we evaluate the enhancement in optical access to the brain upon comparing ex-vivo transmittance measurements of mice native skull and the YSZ cranial implant coupled with scalp and OCAs. Using the transmittance data, the total attenuation lengths were calculated showing that this combination (YSZ and OCAs) offers the best option for gaining improved optical access to the brain.

2. Samples and methods

2.1. Implant fabrication and preparation

Transparent nanocrystalline 8 mol% $YO_1.5$ yttria-stabilized zirconia (YSZ) implant samples were produced from a precursor YSZ nanopowder (Tosoh USA, Inc., Grove City, OH, USA) densified into a transparent bulk ceramic via Current-Activated Pressure-Assisted Densification (CAPAD) procedure developed by Garay et al. and described extensively previously [50, 51].

Biomedical Optics EXPRESS

The thickness of the resulting densified YSZ discs were reduced from 1 mm to approximately 450 μm by polishing with 30 μm diamond slurry on an automatic polisher (Pace Technologies, Tucson, Arizona USA). The samples were then polished with successively finer diamond and silica slurries ranging from 6 to 0.2 μm. Samples were sectioned into rectangles of approximately 2.6 x 2.1 mm using a diamond lapping saw (WEIYI DTQ-5, Qingdao, China), followed by sonication in acetone and thorough rinsing in water. The final thickness of the implants was 440±1 μm.

2.2. Scalp and skull samples

The tissue samples were obtained from animals from the University of California, Riverside (UCR). All experimental procedures and humane care of mice were conducted under a protocol approved by UCR's Institutional Animal Care and Use Committee, and in conformance with the Guide for the Care and Use of Laboratory Animals published by the National Institutes of Health (NIH Publication No. 85-23, revised 1996). The N=9 8-12 week old C57Bl/6 male mice (Jackson Laboratory) used in this study were housed under a 12-hour light and 12-hour dark cycle with *ad libitum* access to food and water.

2.3. Surgical procedures

Craniectomy surgery was conducted as previously described [39]. Briefly, mice were anesthetized with isoflurane inhalation (0.2-0.5%), and given ketamine and xylazine (K/X) (80/10 mg/kg, i.p.). Additional anesthetic was administered as necessary. Hair was removed from the scalp using clippers and depilatory cream. Mice were then secured into stereotaxic frames to immobilize the head for surgery. Ophthalmic ointment was placed over the eyes, and the surgical site was sterilized with alternating application of betadine and 70% EtOH (3 times). A sagittal incision was made to the left of the midline, and the scalp excised to expose the skull. Periosteum was removed from the skull, and a craniectomy was performed with a surgical drill and carbide burr to remove a square section of skull over the right parietal lobe, with dimensions slightly larger than the implant (2.6 x 2.6 mm).

2.4. Optical clearing

A mixture of two biocompatible agents, PEG-400 (PEG) and Propylene Glycol (PG) (Fisher Scientific, California, US), were used as scattering reducer and penetration enhancer, respectively, at a volume ratio of 9:1 [52, 53]. The OCA was prepared and topically applied at room temperature. A thin layer of the OCA was applied on the sample and remained for 50 minutes [52]. Characterization experiments were performed before and immediately after applying the OCA; the increase in transmittance for each tissue used in the samples was monitored every minute over a 50-minute period. For our experimental conditions, the maxima in transmittance were achieved within 50 minutes.

2.5. Tissue characterization

Optical transmittance measurements of the different samples used in this study were obtained through optical spectrometry in the NIR. The setup used to obtain the transmittance spectra incorporates two multimode optical fibers (P400-2-VIS-NIR, Ocean Optics, FL) attached to individual fiber holders including VIS-NIR collimating lenses (MP-74-UV, Ocean Optics, FL, with focal length $f = 10mm$, lens diameter $D = 5mm$ and $NA = D/2f = 0.4$). As depicted in Fig. 1, the holders were attached to a mechanical rail allowing to adjust the separation between the fibers and to allocate a sample holder. After the sample is fixed, the fiber holders were tightly joined together to mitigate detrimental effects from ambient light and back reflections. The light source used for these measurements was a visible-NIR source (HL2000 FHSA, Ocean Optics, FL) launched into one of the optical fibers. The beam exiting the launching fiber then traverses

Biomedical Optics EXPRESS

the sample and is collected by the other fiber, which is connected to a solid-state spectrometer (NIRQUEST 520, Ocean Optics, FL) to obtain the optical transmission spectra. Spectra were acquired averaging 10 measurements, with an integration time of 300 ms, in the 900-2400 nm wavelength range.

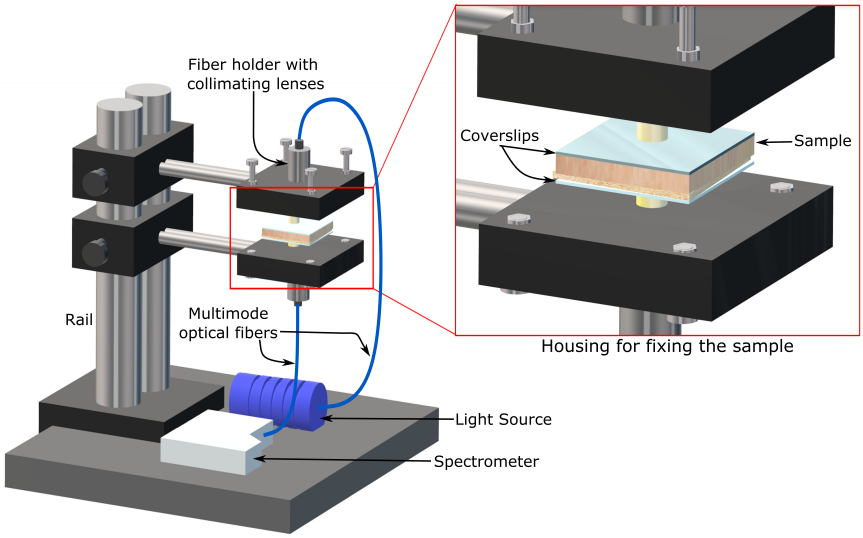

Fig. 1. Collimated transmittance measurements setup. The inset shows the housing for fixing the sample, i.e., the fiber holders with the VIS-NIR collimating lenses. As seen in the inset, the samples are placed between coverslips (see text for further details).

For all the measurements, the collimated transmittance ($T(\lambda)$) was calculated as the ratio of light transmitted through the sample to the total incident light, i.e.:

$$T(\lambda) = \frac{S(\lambda) - D}{I(\lambda) - D} \tag{1}$$

where λ is the wavelength, S is the measured spectral intensity, I is the total light incident and D represents the reference reading under dark conditions (i.e., no light impinging on the sample). Basic models of light propagation in biological tissues are described in terms of radiation transport in a random inhomogeneous media, which includes ballistic and diffuse light [2,5,8,54]. However, when using a collimated beam, and in the case of thin samples with large absorption coefficients and relatively small light scattering, the ballistic part plays a dominant role and the diffusive part is negligible [2, 8, 54]. We further consider that the ballistic photons in the scattering samples are governed by the Beer-Lambert law. Hence, for analyzing the influence of the sample thickness z in the spectral transmittance, the total attenuation length ($l_t(\lambda)$) was calculated as [2, 5, 8, 54]:

$$l_t(\lambda) = \frac{z}{-ln(T(\lambda))} \tag{2}$$

Note that the attenuation length takes into account the sample thickness and therefore provides a better insight of the light penetration through the samples. In particular, for our experiments, the thicknesses of the samples are: $440 \pm 1\mu m$, $159 \pm 1\mu m$ and $710 \pm 20\mu m$ for the YSZ implant, the mice skull and scalp, respectively. Hence, the YSZ implant is 2.5 times thicker than the mice skull.

Biomedical Optics EXPRESS

2.6. Experimental method

The experimental procedure for measuring the ballistic transmittance through the different tissues and the implant was similar to those reported previously for spectroscopic measurements on soft tissue [5, 8, 54]. Transmittance measurements were obtained for three sets of samples arranged as the different scenarios illustrated in Fig. 2. Spectra were obtained first for the skull and subsequently for the stacked array formed by the scalp placed on top of the skull. The OCAs were then applied on the scalp and the spectral transmittance was acquired once again. This set of measurements were also performed using the YSZ implant instead of the skull. The stacking arrangement used for this measurements allowed for evaluating the effects of each layer on the spectral features of the sample. This further allows for comparing the spectral features of the skull and the YSZ implant under similar conditions. Excised full thickness scalp and forehead cranial bone were rinsed briefly in saline solution to remove the excess blood and their thicknesses were measured before placing them in the stacked samples. These were finally placed between two glass microscope coverslips to obtain the transmittance spectra. The same procedure was followed for the YSZ implant. For the cleared skin measurements the scalps were topically exposed to PEG and PG as a scattering reducer and a penetration enhancer, respectively [52, 53].

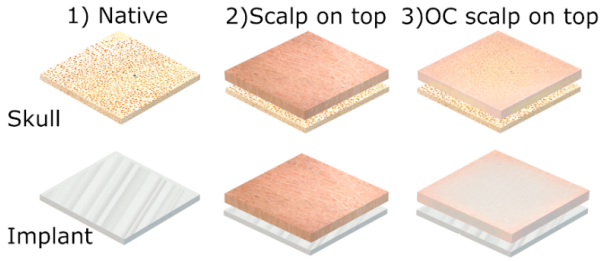

Fig. 2. Stacked sample arrangement used to obtain the spectral transmittance of: 1) the native skull and YSZ implant, 2) the scalp on top of the skull and the YSZ implant, 3) optical cleared (OC) scalp on top of native skull and implant.

3. Results and discussion

Figure 3 shows the transmittance ($T(\lambda)$) and the attenuation length ($l_t(\lambda)$) calculated for the native skull and the implant. The transmittance measurements (Fig. 3(a)) show that the YSZ implant is more transparent throughout the tested NIR range (900-2400 nm) including all of the optical windows commonly used for biophotonic applications (i.e., NIR I, NIR II, SWIR I and SWIR II). This is due to the significant reduction in scattering and absorption when using the YSZ implant. In terms of relative differences in the optical properties between skull and the implant, the latter improves the light transmission within the water absorption bands owing to its reduced water content compared to the native skull (70-75%) [5]. The skull transmittance shows the typical water absorption bands in the NIR spectral region (1450 nm and 1940 nm [9, 10]), while the YSZ implant shows improved transmittance in these bands. The water absorption peaks apparent in the implant spectrum are due to traces of the saline solution used for rinsing aiming at obtaining a fair comparison with the treated tissue samples. A simple calculation of the increase of light transmitted in these bands using the YSZ implant compared to the native skull yields values of 47% at 1450 nm and 53% at 1940 nm. The resulting attenuation length shown in Fig. 3(b) further indicates that, even for the spectral regions with the smallest increase in transmission (e.g., 3% at 1300 nm), light can penetrate deeper when compared to the native skull. Clearly, with exception of the second water absorption band, the attenuation length obtained with the implant increases at least by 1.3 mm, i.e., a four-fold increase in length compared to the skull.

Biomedical Optics EXPRESS

The spectral regions covered by the water absorption peaks in the NIR have not been explored for through-skull techniques because of its high water content. Thus, the improved transmission obtained with the implant opens the possibility to explore new techniques in these wavelength ranges.

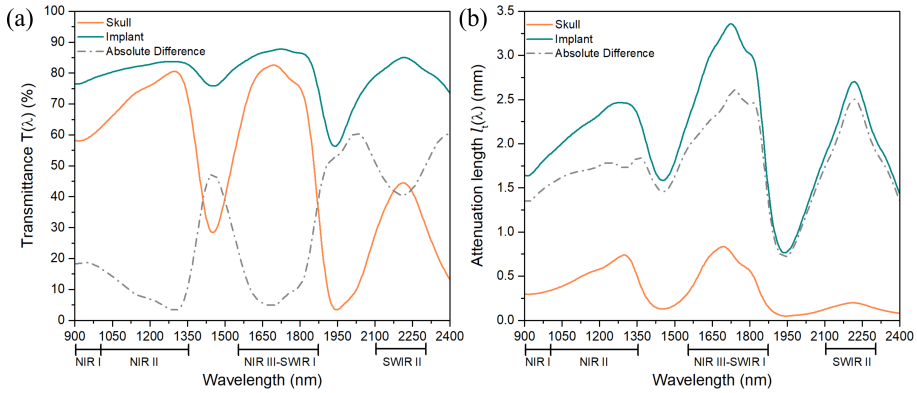

Fig. 3. Transmittance (a) and total attenuation length (b) for the skull and the YSZ implant. The YSZ implant shows better transmittance throughout the full 900-2400 nm spectral range compared to the native skull.

The effect of the scalp on the spectra is evident in Fig. 4(a), showing a considerable reduction in transmission owing to the increased scattering inherent to this tissue [1–3]. As shown in Fig. 4(b), this leads to reduced attenuation lengths for both sample arrangements, i.e., scalp either on top of the skull or on the YSZ implant. Although for both cases the scalp stacking leads to a reduction in transmittance of at least 60%, the sample with the implant still provides the best performance, as confirmed by the attenuation length. Throughout all the spectral range, the sample formed with the scalp and the YSZ implant provides improved light penetration. Clearly, the scalp introduces large optical attenuation effects that must be overcome for the implant to become a convenient means to obtain access for non-invasive optical techniques for post-operatory diagnostics and/or therapeutic purposes. Hence, we evaluated the use of OCAs as a technique for improving the transmittance of the samples.

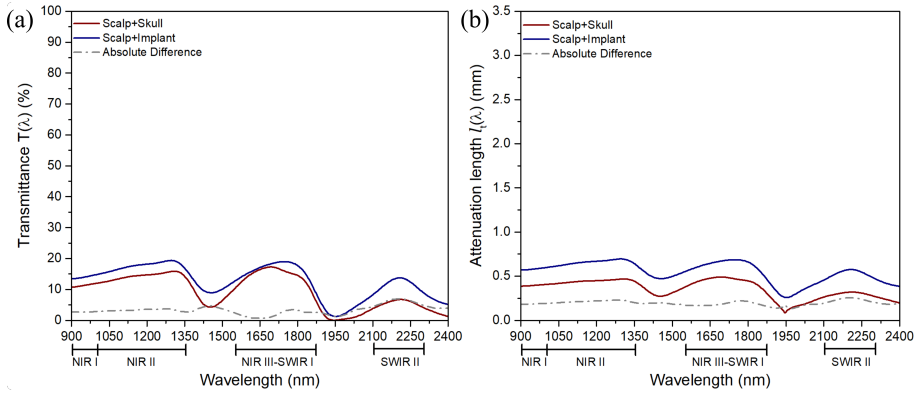

Fig. 4. Transmittance (a) and total attenuation length (b) comparing the stacked samples of the scalp on top of the skull and on the YSZ implant. The sample with the YSZ implant still shows better transmittance and improved attenuation length compared to the sample with the native skull; however, the enhancement is only of 6% in the best case.

Biomedical Optics EXPRESS

The effects of applying a layer of OCAs on the scalp are evident in Fig. 5; the transmittance spectra increases by 20% for the sample with the skull, while for the YSZ implant the enhancement is 40% (Fig. 5(a)). As shown in Fig. 5(b), the attenuation length for both samples increases accordingly; when compared to the results shown in Fig. 4(b), it is clear that the OCAs effectively enhance the light penetration yielding larger attenuation lengths throughout the whole NIR range for both samples. Further comparison of this parameter for the two samples show that the YSZ provides improved light penetration than attained with the skull (up to 1.8 mm more at 1717 nm). These results are consistent with previous reports involving OCAs [40–42], and further confirm that together with the YSZ implant, these biocompatible agents provide attractive features for optical access to the brain tissue without scalp removal.

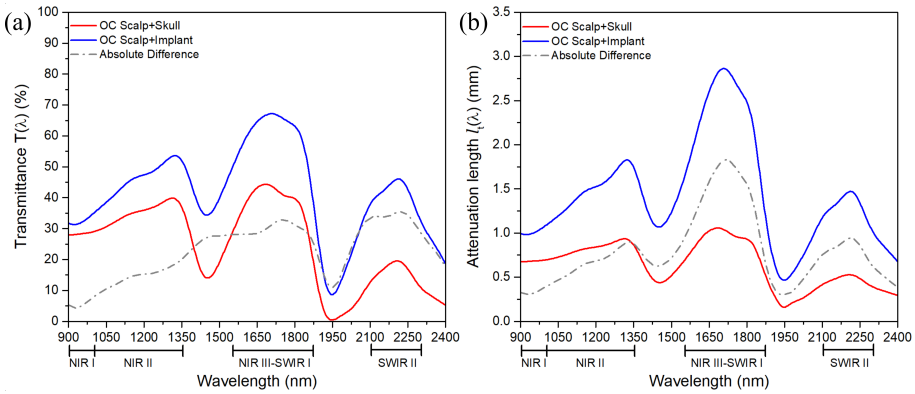

Fig. 5. Transmittance (a) and total attenuation length (b) comparing the stacked samples of the scalp on top of the skull and on the YSZ implant after using the OCAs. The sample using the YSZ implant with optically cleared scalp (OC scalp) shows an increase of up to 30% in transmittance compared to the sample with the skull.

A better idea of the impact of our results in each of the NIR optical windows can be appreciated in Fig. 6, showing a summary of the transmittances and attenuation lengths obtained from our experiments. Comparing all the scenarios, the YSZ implant provides the best option for optical access, showing the largest transmittance and attenuation length. Although the transmittance for the YSZ is seemingly comparable to that of the skull for the NIR II and NIR III windows, the attenuation lengths for the implant are clearly larger than those obtained for the skull (Fig. 6(b)). In fact, for all the windows, the YSZ implant offers improved features and thus better potential for deeper optical access to the brain tissue, even when using the scalp on top. When using OCAs to reduce the scattering of the scalp, the YSZ implant offers improved transmittance and larger attenuation lengths than those observed for the skull. Remarkably, the attenuation lengths achieved with the OCAs and the YSZ show at least a two-fold increase for the last three windows (i.e., NIR II, NIR III-SWIR I and SWIR II). Evidently, the optical features offered by the YSZ implant together with the use of biocompatible agents to reduce scalp scattering pose new possibilities for probing brain tissue in spectral regions that are commonly discarded owing to the low penetration depths that can be commonly achieved [5]. Note that these results provide a direct comparison of the attenuation lengths achieved when replacing the mice skull by the YSZ implant. It is evident that the transparency of the YSZ implant improves the light penetration, but the ultimate increase in penetration depth achievable will depend on the scattering features of the specific bone tissue. Further considerations for the analysis of the spectral transmission should include the diffuse light component, which is relevant when using thicker and more absorbent tissue samples (e.g., rat skull [5]).

Biomedical Optics EXPRESS

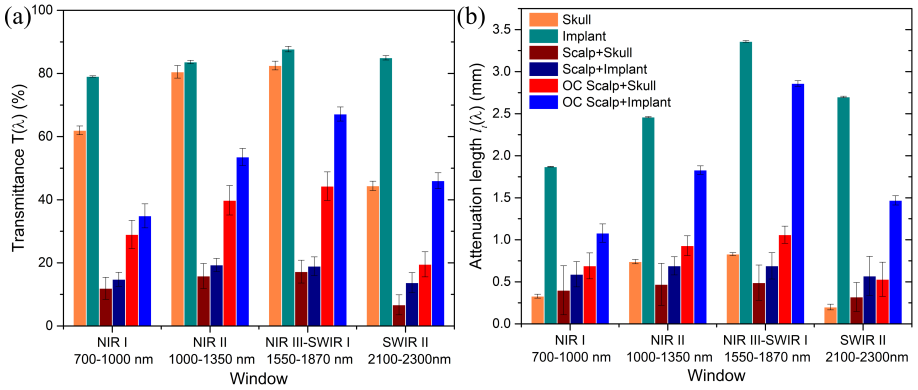

Fig. 6. Summary of the registered transmittance (a) and total attenuation length (b) for the different samples tested in our experiments. Throughout the whole NIR spectral range the YSZ implant shows enhanced transmittance among all the samples. The use of OCAs on the scalp effectively increases both, the transmittance and the attenuation length, providing enhanced light penetration. The most favored optical window for the stacked sample of optically cleared scalp on top of the YSZ implant is the NIR III (1550-1870 nm, T=67%, l_t = 2.86 mm). Error bars represent standard deviation (n=3).

The enhanced transparency of the YSZ implant coupled with the OCAs shows promising features to facilitate various NIR techniques for theranostics. Photobiomodulation (600-1064 nm) [43–45], NIR and fluorescence imaging (700-1700 nm) [3, 46], as well as some types of cancer diagnosis (1500-1800 nm) [47, 48] and brain edema [49] are a few examples of optical techniques that could benefit from the improved transmission in NIR spectral range offered by the YSZ implant. Additionally, any potential adhesion of biochemical agents and/or tissue growth on the implant (e.g., fibrotic tissue, proteins, cell adhesion) could be potentially monitored over time using IR reflection techniques [55]. Imaging techniques (e.g., LSI, fluorescence, absorption) that have been successfully demonstrated to improve with clearing and thinning skull methods [22], may also benefit from the combination of the OCAs and a transparent YSZ implant.

4. Conclusions

We have evaluated the optical transmission and attenuation length of a novel YSZ-based implant intended for chronic optical access to the brain performing *ex-vivo* transmittance measurements. In addition, the use of OCAs to overcome the low transparency of the scalp was explored together with the implant. Direct comparison of the YSZ implant with mouse skull in different stacked arrangements showed that this ceramic material offers enhanced transmission throughout the NIR spectral range. Furthermore, since OCAs effectively reduce the scattering features of the scalp, the use of these biocompatible agents together with the YSZ implant provide improved optical features. In particular, when compared to a typical arrangement comprised of scalp and native skull, the use of the YSZ implant yields an increase in transmittance of up to 50% and attenuation lengths of up to 2.4 mm (i.e., a five-fold increase in light penetration). These experimental results show evidence that the YSZ implant, when used together with the OCAs, offers the best option for gaining improved optical access to the brain. This novel approach seeks to provide new opportunities for monitoring brain conditions on a chronically recurring basis, without requiring repeated craniotomies or scalp removal. Although this study represents only the first step towards the application of NIR optical techniques for brain theranostics through an implant, it offers a relevant insight of the opportunities that this transparent material may eventually provide.

Biomedical Optics EXPRESS

Funding

Conacyt-FONCICYT (246648); Conacyt-'Beca Mixta'(741249); National Science Foundation (NSF) (NSF-PIRE 1545852, NSF-EAGER 1547014).

Acknowledgments

The authors would like to thank Gottlieb Uahengo for the fabrication of the YSZ samples.

Disclosures

The authors declare that there are no conflicts of interest related to this article.

References

1. S. L. Jacques, "Optical properties of biological tissues: a review," Phys. Med. Biol. **58**, R37–61 (2013).
2. L. A. Sordillo, Y. Pu, S. Pratavieira, Y. Budansky, and R. R. Alfano, "Deep optical imaging of tissue using the second and third near-infrared spectral windows," J. Biomed. Opt. **19**, 056004 (2014).
3. G. Hong, A. L. Antaris, and H. Dai, "Near-infrared fluorophores for biomedical imaging," Nat. Biomed. Eng. **1**, 0010 (2017).
4. A. N. Bashkatov, K. V. Berezin, K. N. Dvoretskiy, M. L. Chernavina, E. A. Genina, V. D. Genin, V. I. Kochubey, E. N. Lazareva, A. B. Pravdin, M. E. Shvachkina, P. A. Timoshina, "Measurement of tissue optical properties in the context of tissue optical clearing," J. biomedical optics **23**, 091416 (2018).
5. S. Golovynskyi, I. Golovynska, L. I. Stepanova, O. I. Datsenko, L. Liu, J. Qu, and T. Y. Ohulchanskyy, "Optical windows for head tissues in near-infrared and short-wave infrared regions: Approaching transcranial light applications," J. biophotonics **11**, e201800141 (2018).
6. S. J. Madsen, *Optical Methods and Instrumentation in Brain Imaging and Therapy* (Springer Science & Business Media, 2012).
7. G. Hong, S. Diao, J. Chang, A. L. Antaris, C. Chen, B. Zhang, S. Zhao, D. N. Atochin, P. L. Huang, K. I. Andreasson, C. J. Kuo, and H. Dai, "Through-skull fluorescence imaging of the brain in a new near-infrared window," Nat. Photonics **8**, 723–730 (2014).
8. L. Shi, L. A. Sordillo, A. Rodríguez-Contreras, and R. Alfano, "Transmission in near-infrared optical windows for deep brain imaging," J. Biophotonics **9**, 38–43 (2016).
9. J. A. Curcio and C. C. Petty, "The near infrared absorption spectrum of liquid water," J. Opt. Soc. Am., JOSA **41**, 302–304 (1951).
10. C.-L. Tsai, J.-C. Chen, W.-J. Wang, and Others, "Near-infrared absorption property of biological soft tissue constituents," J. Med. Biol. Eng. **21**, 7–14 (2001).
11. Y. Tsukasaki, M. Morimatsu, G. Nishimura, T. Sakata, H. Yasuda, A. Komatsuzaki, T. M. Watanabe, and T. Jin, "Synthesis and optical properties of emission-tunable PbS/CdS core–shell quantum dots for in vivo fluorescence imaging in the second near-infrared window," RSC Adv. **4**, 41164–41171 (2014).
12. R. H. Wilson, K. P. Nadeau, F. B. Jaworski, B. J. Tromberg, and A. J. Durkin, "Review of short-wave infrared spectroscopy and imaging methods for biological tissue characterization," J. Biomed. Opt. **20**, 030901 (2015).
13. N. S. James, T. Y. Ohulchanskyy, Y. Chen, P. Joshi, X. Zheng, L. N. Goswami, and R. K. Pandey, "Comparative tumor imaging and PDT efficacy of HPPH conjugated in the mono- and di-forms to various polymethine cyanine dyes: part - 2," Theranostics **3**, 703–718 (2013).
14. H.-T. Xu, F. Pan, G. Yang, and W.-B. Gan, "Choice of cranial window type for in vivo imaging affects dendritic spine turnover in the cortex," Nat. Neurosci. **10**, 549–551 (2007).
15. A. Holtmaat, T. Bonhoeffer, D. K. Chow, J. Chuckowree, V. De Paola, S. B. Hofer, M. Hübener, T. Keck, G. Knott, W.-C. A. Lee, R. Mostany, T. D. Mrsic-Flogel, E. Nedivi, C. Portera-Cailliau, K. Svoboda, J. T. Trachtenberg, and L. Wilbrecht, "Long-term, high-resolution imaging in the mouse neocortex through a chronic cranial window," Nat. Protoc. **4**, 1128–1144 (2009).
16. J. Grutzendler, N. Kasthuri, and W.-B. Gan, "Long-term dendritic spine stability in the adult cortex," Nature **420**, 812–816 (2002).
17. A. B. Parthasarathy, S. M. S. Kazmi, and A. K. Dunn, "Quantitative imaging of ischemic stroke through thinned skull in mice with multi exposure speckle imaging," Biomed. Opt. Express **1**, 246–259 (2010).
18. W.-C. A. Lee, J. L. Chen, H. Huang, J. H. Leslie, Y. Amitai, P. T. So, and E. Nedivi, "A dynamic zone defines interneuron remodeling in the adult neocortex," Proc. Natl. Acad. Sci. U. S. A. **105**, 19968–19973 (2008).
19. P. J. Drew, A. Y. Shih, J. D. Driscoll, P. M. Knutsen, P. Blinder, D. Davalos, K. Akassoglou, P. S. Tsai, and D. Kleinfeld, "Chronic optical access through a polished and reinforced thinned skull," Nat. Methods **7**, 981–984 (2010).
20. J. Wang, Y. Zhang, T. H. Xu, Q. M. Luo, and D. Zhu, "An innovative transparent cranial window based on skull optical clearing," Laser Phys. Lett. **9**, 469 (2012).
21. E. A. Genina, A. N. Bashkatov, and V. V. Tuchin, "Optical clearing of cranial bone," Adv. Opt. Technol. **2008**, 267867 (2008).

Biomedical Optics EXPRESS

22. Y.-J. Zhao, T.-T. Yu, C. Zhang, Z. Li, Q.-M. Luo, T.-H. Xu, and D. Zhu, "Skull optical clearing window for in vivo imaging of the mouse cortex at synaptic resolution," Light. Sci. Appl. **7**, 17153 (2018).
23. C. J. Roome and B. Kuhn, "Chronic cranial window with access port for repeated cellular manipulations, drug application, and electrophysiology," Front. Cell. Neurosci. **8**, 379 (2014).
24. V. Zuluaga-Ramirez, S. Rom, and Y. Persidsky, "Craniula: A cranial window technique for prolonged imaging of brain surface vasculature with simultaneous adjacent intracerebral injection," Fluids Barriers CNS **12**, 24 (2015).
25. C. Heo, H. Park, Y.-T. Kim, E. Baeg, Y. H. Kim, S.-G. Kim, and M. Suh, "A soft, transparent, freely accessible cranial window for chronic imaging and electrophysiology," Sci. Rep. **6**, 27818 (2016).
26. S. S. Smith, P. Magnusen, and B. J. Pletka, "Fracture toughness of glass using the indentation fracture technique," in *Fracture Mechanics for Ceramics, Rocks, and Concrete,* (ASTM International, 1981), pp. 33.
27. S. F. Hulbert, "The use of alumina and zirconia in surgical implants," in *An Introduction to Bioceramics,* (2013), pp. 27–47.
28. A. Sharova, Y. S. Maklygina, G. Yusubalieva, I. Shikunova, V. Kurlov, and V. Loschenov, "Sapphire implant based neuro-complex for deep-lying brain tumors phototheranostics," in *Journal of Physics: Conference Series,* vol. 945 (IOP Publishing, 2018), p. 012009.
29. Y. Damestani, C. L. Reynolds, J. Szu, M. S. Hsu, Y. Kodera, D. K. Binder, B. H. Park, J. E. Garay, M. P. Rao, and G. Aguilar, "Transparent nanocrystalline yttria-stabilized-zirconia calvarium prosthesis," Nanomedicine **9**, 1135–1138 (2013).
30. Y. Damestani, D. E. Galan-Hoffman, D. Ortiz, P. Cabrales, and G. Aguilar, "Inflammatory response to implantation of transparent nanocrystalline yttria-stabilized zirconia using a dorsal window chamber model," Nanomedicine **12**, 1757–1763 (2016).
31. J. E. Alaniz, F. G. Perez-Gutierrez, G. Aguilar, and J. E. Garay, "Optical properties of transparent nanocrystalline yttria stabilized zirconia," Opt. Mater. **32**, 62–68 (2009).
32. S. R. Casolco, J. Xu, and J. E. Garay, "Transparent/translucent polycrystalline nanostructured yttria stabilized zirconia with varying colors," Scr. Mater. **58**, 516–519 (2008).
33. P. Christel, A. Meunier, M. Heller, J. P. Torre, and C. N. Peille, "Mechanical properties and short-term in-vivo evaluation of yttrium-oxide-partially-stabilized zirconia," J. Biomed. Mater. Res. **23**, 45–61 (1989).
34. K. Nakamura, T. Kanno, P. Milleding, and U. Ortengren, "Zirconia as a dental implant abutment material: a systematic review," Int. J. Prosthodont. **23**, 299–309 (2010).
35. P. Christel, A. Meunier, J. M. Dorlot, J. M. Crolet, J. Witvoet, L. Sedel, and P. Boutin, "Biomechanical compatibility and design of ceramic implants for orthopedic surgery," Ann. N. Y. Acad. Sci. **523**, 234–256 (1988).
36. M. I. Gutierrez, E. H. Penilla, L. Leija, A. Vera, J. E. Garay, and G. Aguilar, "Novel cranial implants of Yttria-Stabilized zirconia as acoustic windows for ultrasonic brain therapy," Adv. Heal. Mater. **6** (2017).
37. N. Davoodzadeh, M. S. Cano-Velázquez, D. L. Halaney, C. R. Jonak, D. K. Binder, and G. Aguilar, "Evaluation of a transparent cranial implant for multi-wavelength intrinsic optical signal imaging," in *Neural Imaging and Sensing 2019,* vol. 10865 (International Society for Optics and Photonics, 2019), p. 108650B.
38. N. Davoodzadeh, D. Halaney, C. R. Jonak, N. Cuando, A. Aminfar, D. K. Binder, and G. Aguilar, "Laser speckle imaging of brain blood flow through a transparent nanocrystalline yttria-stabilized-zirconia cranial implant," in *Dynamics and Fluctuations in Biomedical Photonics XV,* vol. 10493 (International Society for Optics and Photonics, 2018), p. 1049303.
39. N. Davoodzadeh, M. S. Cano-Velázquez, D. L. Halaney, C. R. Jonak, D. K. Binder, and G. Aguilar, "Evaluation of a transparent cranial implant as a permanent window for cerebral blood flow imaging," Biomed. Opt. Express **9**, 4879–4892 (2018).
40. V. Tuchin, *Tissue Optics Light Scattering Methods and Instruments for Medical Diagnosis* (SPIE, 2000).
41. V. V. Tuchin, I. L. Maksimova, D. A. Zimnyakov, I. L. Kon, A. H. Mavlyutov, and A. A. Mishin, "Light propagation in tissues with controlled optical properties," J. biomedical optics **2**, 401–418 (1997).
42. E. A. Genina, A. N. Bashkatov, Y. P. Sinichkin, I. Y. Yanina, and V. V. Tuchin, "Optical clearing of tissues: Benefits for biology, medical diagnostics, and phototherapy," in *Handbook of Optical Biomedical Diagnostics*, Second Edition, Volume 2: Methods, V. V. Tuchin, ed. (SPIE Press, 2016).
43. F. Salehpour, F. Farajdokht, P. Cassano, S. Sadigh-Eteghad, M. Erfani, M. R. Hamblin, M. M. Salimi, P. Karimi, S. H. Rasta, and J. Mahmoudi, "Near-infrared photobiomodulation combined with coenzyme Q for depression in a mouse model of restraint stress: reduction in oxidative stress, neuroinflammation, and apoptosis," Brain Res. Bull. **144**, 213–222 (2019).
44. M. A. Caldieraro and P. Cassano, "Transcranial and systemic photobiomodulation for major depressive disorder: A systematic review of efficacy, tolerability and biological mechanisms," J. Affect. Disord. **243**, 262–273 (2019).
45. M. R. Hamblin, "Photobiomodulation for traumatic brain injury and stroke," J. Neurosci. Res. **96**, 731–743 (2018).
46. E. Hemmer, A. Benayas, F. Légaré, and F. Vetrone, "Exploiting the biological windows: current perspectives on fluorescent bioprobes emitting above 1000 nm," Nanoscale Horizons **1**, 168–184 (2016).
47. Z. Xue, S. Zeng, and J. Hao, "Non-invasive through-skull brain vascular imaging and small tumor diagnosis based on NIR-II emissive lanthanide nanoprobes beyond 1500 nm," Biomaterials **171**, 153–163 (2018).
48. D. C. Sordillo, L. A. Sordillo, P. P. Sordillo, L. Shi, and R. R. Alfano, "Short wavelength infrared optical windows for evaluation of benign and malignant tissues," J. Biomed. Opt. **22**, 45002 (2017).
49. J. R. Thiagarajah, M. C. Papadopoulos, and A. S. Verkman, "Noninvasive early detection of brain edema in mice by

Biomedical Optics EXPRESS

near-infrared light scattering," J. Neurosci. Res. **80**, 293–299 (2005).
50. J. E. Garay, "Current-Activated, Pressure-Assisted densification of materials," Annu. Rev. Mater. Res. **40**, 445–468 (2010).
51. N. Davoodzadeh, G. Uahengo, D. Halaney, J. E. Garay, and G. Aguilar, "Influence of low temperature ageing on optical and mechanical properties of transparent yittria stabilized-zirconia cranial prosthesis," in *Design and Quality for Biomedical Technologies XI,* vol. 10486 (International Society for Optics and Photonics, 2018), p. 104860A.
52. R. Shi, L. Guo, C. Zhang, W. Feng, P. Li, Z. Ding, and D. Zhu, "A useful way to develop effective in vivo skin optical clearing agents," J. Biophotonics **10**, 887–895 (2017).
53. D. Zhu, K. V. Larin, Q. Luo, and V. V. Tuchin, "Recent progress in tissue optical clearing," Laser Photon. Rev. **7**, 732–757 (2013).
54. S. A. Filatova, I. A. Shcherbakov, and V. B. Tsvetkov, "Optical properties of animal tissues in the wavelength range from 350 to 2600 nm," J. Biomed. Opt. **22**, 35009 (2017).
55. N. Davoodzadeh, N. Cuando, A. H. Aminfar, M. Cano, and G. Aguilar, "Assessment of bacteria growth under transparent nanocrystalline yttriastabilized-zirconia cranial implant using laser speckle imaging," in *Lasers in Surgery and Medicine,* vol. 50 (Wiley, 2018), pp. S5–S6.